

# Flexible, Printable Soft-X-Ray Detectors Based on All-Inorganic Perovskite Quantum Dots

Jingying Liu, Babar Shabbir,\* Chujie Wang, Tao Wan, Qingdong Ou, Pei Yu, Anton Tadich, Xuechen Jiao, Dewei Chu, Dongchen Qi, Dabing Li, Ruifeng Kan, Yamin Huang, Yemin Dong, Jacek Jasieniak, Yupeng Zhang,\* and Qiaoliang Bao\*

Metal halide perovskites represent a family of the most promising materials for fascinating photovoltaic and photodetector applications due to their unique optoelectronic properties and much needed simple and low-cost fabrication process. The high atomic number ( $Z$ ) of their constituents and significantly higher carrier mobility also make perovskite semiconductors suitable for the detection of ionizing radiation. By taking advantage of that, the direct detection of soft-X-ray-induced photocurrent is demonstrated in both rigid and flexible detectors based on all-inorganic halide perovskite quantum dots (QDs) synthesized via a solution process. Utilizing a synchrotron soft-X-ray beamline, high sensitivities of up to  $1450 \mu\text{C Gy}_{\text{air}}^{-1} \text{cm}^{-2}$  are achieved under an X-ray dose rate of  $0.0172 \text{ mGy}_{\text{air}} \text{s}^{-1}$  with only  $0.1 \text{ V}$  bias voltage, which is about 70-fold more sensitive than conventional  $\alpha\text{-Se}$  devices. Furthermore, the perovskite film is printed homogeneously on various substrates by the inexpensive inkjet printing method to demonstrate large-scale fabrication of arrays of multi-channel detectors. These results suggest that the perovskite QDs are ideal candidates for the detection of soft X-rays and for large-area flat or flexible panels with tremendous application potential in multidimensional and different architectures imaging technologies.

Low-cost X-ray detectors with high performance, durability, and flexibility, are required for a wide range of applications in several fields, such as medical (diagnostic radiology, imaging, etc.), nondestructive testing (radioscopic inspections, radiography testing, etc.), security and defence (baggage/body scanning systems, paper mail, etc.), nuclear and radiation industries (nuclear power plants, research reactors, users of nuclear gauges, etc.), and research and development.<sup>[1]</sup> X-ray detection using semiconductors, based on the direct generation of electrical signals by X-rays (i.e., direct scheme), offers better spatial resolution and a simpler route than indirect schemes, in which X-rays are converted into photons by scintillating phosphors before detection by photodiode arrays.<sup>[2]</sup> Currently, the conventional materials used for direct conversion of X-rays include stabilized amorphous Se ( $\alpha\text{-Se}$ ),  $\text{PbI}_2$ ,  $\text{HgI}_2$ ,  $\text{CdTe}$ , and  $\text{CdZnTe}$ .<sup>[3]</sup>

J. Liu, Dr. B. Shabbir, C. Wang, Q. Ou, P. Yu, Dr. X. Jiao, Prof. J. Jasieniak, Dr. Y. Zhang, Prof. Q. Bao  
Department of Materials Science and Engineering  
Monash University  
Clayton, Victoria 3800, Australia  
E-mail: yupeng.zhang@monash.edu; qiaoliang.bao@monash.edu


Dr. B. Shabbir, Prof. D. Li, Prof. R. Kan  
State Key Laboratory of Applied Optics  
Changchun Institute of Optics  
Fine Mechanics and Physics  
Chinese Academy of Sciences  
Changchun, Jilin 130033, China  
E-mail: bshabbir@ciomp.ac.cn  
T. Wan, Prof. D. Chu  
School of Materials Science and Engineering  
University of New South Wales  
Kensington, Sydney, New South Wales 2052, Australia

Dr. A. Tadich, Dr. X. Jiao  
Australian Synchrotron, ANSTO  
800 Blackburn Road, Clayton, Victoria 3168, Australia

Dr. A. Tadich  
Department of Chemistry and Physics  
La Trobe Institute for Molecular Science  
La Trobe University  
Melbourne, Victoria 3086, Australia

Dr. D. Qi  
School of Chemistry, Physics and Mechanical Engineering  
Queensland University of Technology  
Brisbane, Queensland 4001, Australia

Dr. Y. Huang, Prof. Y. Dong  
State Key Laboratory of Functional Materials for Informatics  
Shanghai Institute of Microsystem and Information Technology  
Chinese Academy of Sciences  
Shanghai 200050, China

 The ORCID identification number(s) for the author(s) of this article can be found under <https://doi.org/10.1002/adma.201901644>.

DOI: 10.1002/adma.201901644

Nevertheless, there are still huge demands to develop detecting materials that are solution processable or processable at low temperatures, and highly sensitive to the low dose of X-rays.<sup>[4]</sup>

High sensitivity of a material is a key parameter for X-ray detectors because it can allow the material to easily detect a small X-ray dose or in other words, reduces ionizing radiation risks.<sup>[5]</sup> Exposure to high doses of X-rays can increase lifetime cancer risk in patients, particularly in children, and exposure of sensitive parts of the adult body to X-rays can double the risk or lead to the development of certain disorders.<sup>[6]</sup> Therefore, X-ray detectors with high sensitivities can largely reduce such risks by minimizing the X-ray dose, while performing various radiological and/or radiographical procedures. Recently, the metal halide perovskites, best known for their exciting use in photovoltaic and optoelectronic applications,<sup>[7]</sup> have revealed a lot of exciting X-ray detection characteristics, such as large X-ray stopping power,<sup>[8]</sup> efficient X-ray generating photocarriers,<sup>[9]</sup> low cost, and simple fabrication, and so on.<sup>[10]</sup> Noticeably, the recently demonstrated X-ray detectors based on organic–inorganic perovskites, for example, MAPbI<sub>3</sub> perovskite thin films<sup>[11]</sup> or MAPbBr<sub>3</sub>/Cs<sub>2</sub>AgBiBr<sub>6</sub> perovskite bulk single crystals<sup>[12]</sup> have shown an ultrahigh sensitivities of  $\approx 10^4 \mu\text{C Gy}_{\text{air}}^{-1} \text{cm}^{-2}$  when exposed to high-energy X-rays, which are significantly higher than commercial  $\alpha$ -Se X-ray detectors. Additionally, high quality or fine images can be easily achieved with relatively low dose exposures, which is another key advantage of perovskite materials.<sup>[8a]</sup> So far, performances for such detectors, whether on rigid or flexible substrates, have not been tested for soft X-rays. It is also challenging to pattern homogenous thin films at the desired location in a large scale, as well as to fabricate the arrays of flexible detectors. Similarly, the diversity of the applications is restricted by the size and the shape of the detector and this innovation requires a shift toward commercial manufacturing and so it implies novel device design and fabrication. Therefore, developing a high-performance, flexible X-ray detector based on low-temperature and solution-processable perovskites and large-scale patterning of homogeneous films with soft X-ray functionalities are of great importance.

Here, we demonstrate a flexible, printable X-ray detector with remarkable soft X-ray detecting functionalities based on high-quality colloidal CsPbBr<sub>3</sub> perovskite QDs, which are synthesized via hot injection method at room temperature. To enhance the crystal sensitivity, we effectively reduced the surface defects and controllably tuned the crystallinity via chemistry engineering. These monocrystalline QDs are phase stable at room temperature and under illumination in comparison with other organic–inorganic perovskites.<sup>[13]</sup> Therefore, they can sustain high performance in terms of optoelectronic functionalities under various stress conditions. It is found that our X-ray detectors operate at a very low voltage and are 70-fold more sensitive than conventional  $\alpha$ -Se devices. It is noteworthy that this solution-processed perovskite can be used as inks for inexpensive inkjet printing. This makes the patterning of CsPbBr<sub>3</sub> perovskite QDs scalable and that eventually demonstrates a scalable production of large-area detector arrays with remarkable soft X-ray detecting functionalities.

**Figure 1a** illustrates our approach to fabricate large-area X-ray detector arrays using the solution of CsPbBr<sub>3</sub> QDs via

inkjet printing on SiO<sub>2</sub>/Si substrate. More specifically, the SiO<sub>2</sub>/Si or flexible poly(ethylene terephthalate) (PET) substrate was predeposited with gold counter electrodes via photolithography and electron beam evaporation (see Figure S1 in the Supporting Information). Then, the QDs film was printed in the middle of the counter electrode pairs by an inkjet printer using CsPbBr<sub>3</sub> QDs solution as ink. During the printing process, the solution was aggregated along the droplet periphery, which resulted in an inhomogeneous distribution of the material by the coffee ring effect. Subsequently, after the complete solvent evaporation at room temperature, the continuous thin perovskite film would be formed in a parallel structure comprising Au/CsPbBr<sub>3</sub>/Au (see Figure 1c). From the micro photoluminescence (PL) mapping image shown in Figure 1d, we can see that the CsPbBr<sub>3</sub> perovskite film with high PL intensity was more uniform than the spin-coated one. Due to the wettability difference between Au electrodes and SiO<sub>2</sub> surface, the droplets tend to spread on the substrate in different contact angles, leading to the thickness difference across the film on Au and SiO<sub>2</sub>. To confirm the detailed morphology of the as-printed perovskite film, the topography and thickness of the perovskite film were investigated by atomic force microscope (AFM), as shown in Figure 1e. It is found that the thickness of the film is around 20 nm and the surface roughness is around 4 nm. More importantly, we can also integrate the X-ray detector arrays onto a 4 inch large SiO<sub>2</sub>/Si wafer substrate (Figure 1b) to realize the development of advanced next-generation optoelectronic devices.

The CsPbBr<sub>3</sub> QDs were synthesized by a well-developed hot injection method (see the Experimental Section) carrying out on a standard Schlenk line.<sup>[14]</sup> To characterize the crystal structure and microstructure of perovskite QDs, powder X-ray diffraction (XRD) and transmission electron microscopy (TEM) were performed. Figure 1f shows the XRD results of CsPbBr<sub>3</sub> QDs deposited on a glass substrate. The inset of Figure 1f shows the typical crystal structure of the CsPbBr<sub>3</sub> perovskite, comprising corner-sharing PbX<sub>6</sub> octahedra with Cs<sup>+</sup> ions filling the voids in between. From the XRD patterns, three dominant diffraction peaks at 15°, 21.5°, and 30.5°, which can be assigned to the (100), (110), and (200) facets, respectively, demonstrated the cubic perovskite crystal structure of the *Pm3m* CsPbBr<sub>3</sub> QDs. Additionally, TEM was performed to identify the structural characteristics of the CsPbBr<sub>3</sub> QDs. The monodisperse CsPbBr<sub>3</sub> exhibited a cubic shape in Figure 1g with an average edge length around 10 nm. The phase structure of the as-synthesized QDs can be further identified by high-resolution transmission electron microscopy (HRTEM) image of single CsPbBr<sub>3</sub> QD. It can be observed in Figure 1h that these QDs possess interplanar distance of  $\approx 0.58$  nm, which is consistent with the lattice space of (100) plane of the  $\alpha$ -phase CsPbBr<sub>3</sub>.

The optical properties of the CsPbBr<sub>3</sub> QD solution and film are further investigated by utilizing the ultraviolet–visible (UV–vis) absorption and PL spectroscopies. The film was produced by directly drop casting the QDs solution on a glass substrate. The comparison of the UV–vis absorption and PL spectra of CsPbBr<sub>3</sub> QDs in solution and film are shown in Figure 1i. The as-synthesized perovskite QDs exhibit band-edge absorption approaching the bulk optical bandgap of 2.3 eV, which is similar

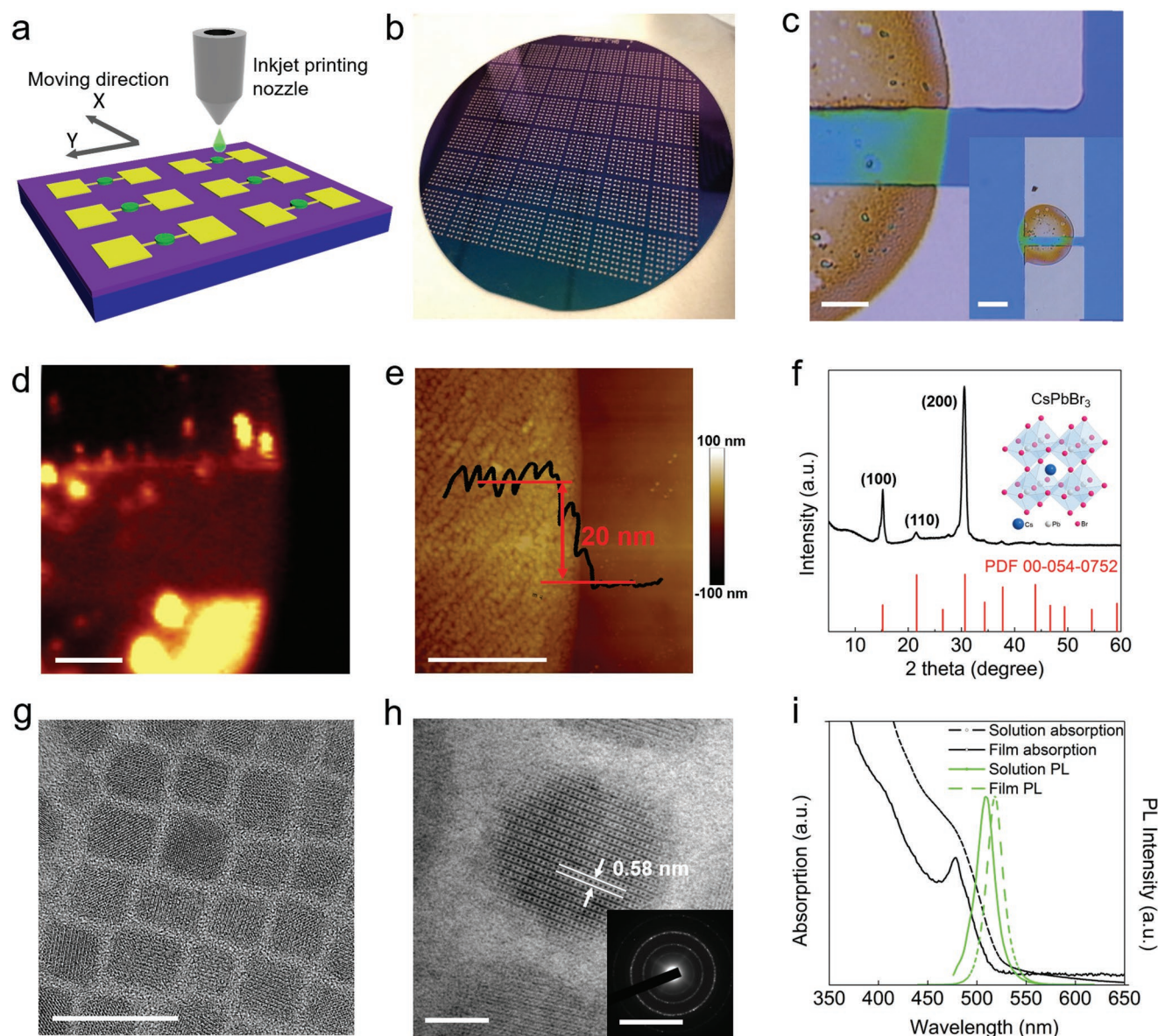


**Figure 1.** Characterization of perovskites. a) Schematic illustration of the key fabrication procedures for perovskite-based devices via inkjet printing. b) Photograph of X-ray detector arrays on 4 inch wafer. c) Optical image of device with printed QDs film. Scale bar: 5 μm. Inset: low-magnification image. Scale bar: 50 μm. d) PL mapping image of region shown in (c). Scale bar: 5 μm. e) AFM height image of the printed QDs film. Scale bar: 5 μm. f) Powder X-ray diffraction pattern of CsPbBr<sub>3</sub> QDs with standard spectra. Inset: crystal structure of CsPbBr<sub>3</sub>. g) TEM image of CsPbBr<sub>3</sub> QDs. Scale bar: 20 nm. h) High-resolution TEM of CsPbBr<sub>3</sub> QDs. Scale bar: 5 nm. Inset: Selected-area diffraction image. Scale bar: 5 1/nm. i) UV-vis absorption and PL spectra for CsPbBr<sub>3</sub> QDs solution and film, respectively.

to the optical features of previous reports.<sup>[15]</sup> Furthermore, the perovskite QDs film shows an absorption edge at 483 nm while the PL peak of the perovskite film is located at 510 nm. There exists a small red shift ( $\approx 7$  nm) in the PL spectrum of the film compared to that of solution. The QDs with similar size self-assemble together and pack more closely during the film formation. Thereby, the emissions from the small particles, which have larger energy and smaller wavelength, would have a high chance of being absorbed by the larger particles, resulting the PL spectrum of the film redshifted. The PL spectrum is a good Gaussian curve and its full-width at half-maximum (FWHM) is  $\approx 25$  nm, giving high-purity green emission. No sub-bandgap

emission was observed in these PL spectra, indicating the pure phase of CsPbBr<sub>3</sub> QDs both in solution and film.

To study the detection performance, we expose our device under the synchrotron soft X-ray beamline with photon energies ranging from 0.1 to 2.5 keV. **Figure 2a** is the schematic of an experimental setup used for the soft-X-ray-induced photocurrent measurements at the soft-X-ray beamline in Australian Synchrotron. Contrary to a conventional X-ray beam, synchrotron radiation is highly collimated with large photon flux, excellent energy resolution, and controlled dose rates.<sup>[16]</sup> The actual dose rate of the X-ray radiation exposure to the sample was measured by a Radcal dosimeter (see the Experimental Section)



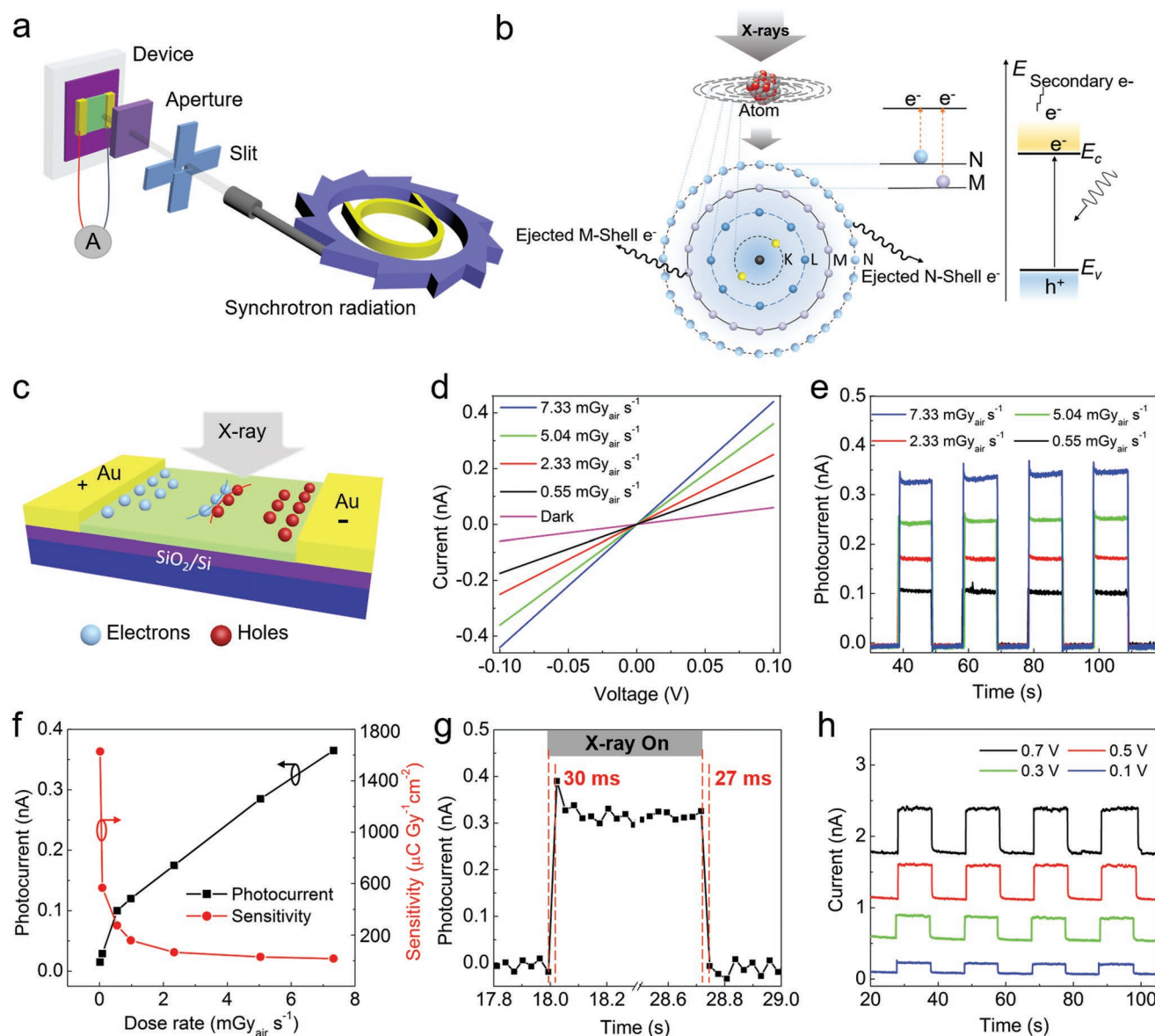


**Figure 2.** Soft-X-ray detection on synchrotron radiation. a) Layout of the Australian Synchrotron Facility and experimental setup for the synchrotron X-ray detecting measurements. b) Mechanism investigation on X-ray photon to current conversion by CsPbBr<sub>3</sub> QDs film. c) Schematic illustration of configuration and working principle of the X-ray detector. d) *I*–*V* curve under X-ray with different dose rate with 0.1 V bias voltage. e) Device response to X-ray on turning the X-ray source on and off under different dose rates with 0.1 V bias voltage. f) X-ray photocurrents and sensitivity as a function of dose rate with 0.1 V bias voltage. g) Temporal response of device under 7.33 mGy<sub>air</sub> s<sup>−1</sup> dose rates with 0.1 V bias voltage. h) Device response to X-ray pulse with varying applied bias voltage under 7.33 mGy<sub>air</sub> s<sup>−1</sup> dose rates.

placed at the sample position (the same distance between sample and beam). The configuration and the working principle of the X-ray detector are illustrated in Figure 2c. The detection of X-ray requires the interaction between the X-ray and a volume of material, creating free electrons that can be ultimately detected as electric current. As CsPbBr<sub>3</sub> absorbs the energy of the incident X-ray photons, it will provide electron–hole pairs to induce photocurrent during the interaction between the X-ray and the perovskite QDs. Here, the X-ray-induced excitons in the perovskite device were experimentally measured by the current through the device under the X-ray illumination. The external bias voltage applied to the depth of the perovskite layer could

draw the electrons and holes to the corresponding electrodes, which helps efficient charge collection from the X-ray detector. Therefore, a source meter was linked to applying voltage to the device and output current from the device.

Figure 2d presents the typical *I*–*V* curves of the X-ray detector device under the irradiation of soft X-rays with different dose rates with a 0.1 V bias voltage applied. Clearly, the *I*–*V* curve shows a linear dependence on the applied voltage (−0.1–0.1 V), indicating an Ohmic contact between the perovskite and gold electrodes. The X-ray-induced current was found to increase from 0.1 to 0.36 nA as the dose rate of the X-ray increased from 0.55 to 7.33 mGy<sub>air</sub> s<sup>−1</sup> (entrance dose in the

air), which is attributed to the strong interaction between the soft X-ray and perovskite. The time-dependent X-ray response (Figure 2e) for our device was investigated to determine the stability and reproducibility of the signal by repeatedly turning the incident X-ray on and off to certain X-ray dose rate. The device was exposed for 10 sec under X-ray with 10 sec resting period between each exposure. Despite the photocurrent being slightly increased under the dose rate of  $7.33 \text{ mGy}_{\text{air}} \text{ s}^{-1}$ , it remained nearly constant at the other three different dose rates, indicating this X-ray detector presents good stability over the period of exposure. To evaluate the sensitivity of the CsPbBr<sub>3</sub> perovskite-based X-ray detector, the slope of the device output photocurrent versus X-ray dose rate was calculated. The measured photocurrent was almost linear with the X-ray dose rate at the high range ( $0.5\text{--}7 \text{ mGy}_{\text{air}} \text{ s}^{-1}$ ) indicating the great potential of the detector in accurate radiation measurements in sensitive radiation areas (Figure 2f). The highest sensitivity of this X-ray detector was calculated to be  $1450 \mu\text{C Gy}_{\text{air}}^{-1} \text{ cm}^{-2}$  at 0.1 V bias obtained from the device under the X-ray with the dose rate  $0.0172 \text{ mGy}_{\text{air}} \text{ s}^{-1}$  and photocurrent about 0.09 nA. This is much higher compared with that of amorphous Se ( $1\text{--}20 \mu\text{C mGy}_{\text{air}}^{-1} \text{ cm}^{-2}$ ), a crucial material for commercial flat-panel-based X-ray imaging. These results clearly suggest the great potential of CsPbBr<sub>3</sub> for direct conversion of X-ray into electrical signals (Table S1, Supporting Information).

The short pulse of the response is shown in Figure 2g. The rising (reaching 90% of the saturated X-ray signal) and falling (reaching 10% of the saturated X-ray signal) times of the detector based on perovskite QD film under 0.1 V bias are about 30 and 27 ms, respectively, showing a relatively fast response time. Figure 2h plots the current signals of the detector under the same dose rate of  $7.33 \text{ mGy}_{\text{air}} \text{ s}^{-1}$  for four different bias voltages. It is obvious that the current rises with the enhanced bias voltage, which may contribute to enhance the charge separation by the external electrical field. On the other hand, the difference between the current is slightly dependent on the bias voltage at a constant dose rate. Thus, we can also improve the sensitivity of the detector by increasing the bias voltage during the operation of the X-ray detector. For measurement of radiation energies above 2.5 keV, we further tested our device under standard lab-based X-ray diffraction conditions, which has a higher photon energy than the synchrotron soft-X-ray beamline. As it can be seen in Figure S2 in the Supporting Information, although the photocurrent is much higher, its sensitivity is much lower ( $<10 \mu\text{C Gy}_{\text{air}}^{-1} \text{ cm}^{-2}$ ).

We further proposed the possible mechanism of the detecting process in Figure 2b. The above results of the X-ray detector can be explained by considering the quantum efficiency of the internal photoelectric effect. According to quantum theory, the wavelengths of the X-ray are on the order of the size of atoms. As a result, they look less like waves and more like particles, or called photons, i.e., the smallest possible unit of the radiation. In fact, the interaction between the X-ray photons and electrons in atoms dominates the interaction between the X-ray and perovskite QDs film. When the perovskite layer absorbs the X-ray photon energy, high-energy electron-hole pairs will be generated. To be exact, when the X-ray photons pass through the atom, they interact with the electrons (in electron shells of the atoms) in the form of collision, during which

part of the photon energy will be transferred to those bound electrons, while the rest energy is converted into kinetic energy of these electrons. In this case, the number of electrons that leaves the atoms depends both on the absorbed photon energy and detecting materials. The efficiency can be defined as the number of electron-hole pairs generated per one X-ray photon absorbed in the detector. The binding energies of electrons on K, L, M, and N shell in free Cs, Pb, and Br atoms are listed in Table S2 in the Supporting Information. For example, when a very low energy X-ray (100 eV) interacts with the CsPbBr<sub>3</sub> perovskite, there will be a high possibility of some electrons in N and O shell of the Cs, O shell of Pb, and M shell of the Br to be knocked out. The higher the X-ray energy that is used, the higher the kinetic energy of electrons that are knocked loose from its atom shell and escaped from the atoms (depending on the binding energies). When these photoelectrons move freely in the lattices, they can be considered as secondary electrons, which are then mostly relax into conduction band edge. In the meantime, the high energy of X rays can readily excite the optical bandgap of CsPbBr<sub>3</sub> perovskites, producing enough charge carriers in the valence band and conduction band after multiple relaxation processes. Moreover, the bias voltage will induce the electric field in the materials, which increases the kinetic energy of the photoelectrons, thus, improving the sensitivity of the X-ray detector.

The flexibility and durability of the CsPbBr<sub>3</sub> perovskite-based X-ray detectors were also investigated. A schematic of the flexible perovskite device array is presented in Figure 3a. To develop flexible optoelectronic devices, perovskite device arrays were fabricated by printing CsPbBr<sub>3</sub> thin film from solution onto the flexible PET substrate similarly as mentioned above. Due to the different wettability of the substrate, the printed film on PET was thinner than that on the SiO<sub>2</sub>/Si substrate. Therefore, the dark current (Figure S3, Supporting Information) was much lower than that of the device on SiO<sub>2</sub>/Si substrate. The bending test of the X-ray detector device on the PET substrate was performed with different bending angles. As we can see from Figure 3b, due to the good mechanical flexibility of the PET substrate underlay, the real flexible device can be bent easily in various angles. The X-ray response of the flexible device was evaluated in the form of current under X-ray irradiation at different bending angles and after hundreds of bending cycles. Figure 3c illustrates the current of the CsPbBr<sub>3</sub> perovskite-based X-ray detector arrays as a function of the voltage (0–1 V) under the exposure of X-ray radiation ( $7.33 \text{ mGy}_{\text{air}} \text{ s}^{-1}$ ) at different bending angles. The inset is the image of our homemade loading frame setup for bending test at a 120° bending angle. As it can be seen from the Figure 3c, the current was reduced about 25% at the 120° angle, which was probably due to the 80% reduction of incident X-ray radiation due to severe bending. Furthermore, the durability of the flexible detector was measured against the bending cycles. Generally, a little strain either caused by doping<sup>[17]</sup> or stress<sup>[18]</sup> can significantly change the material properties. On the contrary, the strain produced via 200 bending cycles degraded the current by only 12% (see Figure 3d), which indicates its excellent conductivity, stability and durability, and it could be linked to uniformly growth of the perovskite film via printing. These exciting results indicate the high robustness and stability of our X-ray detector. Considering

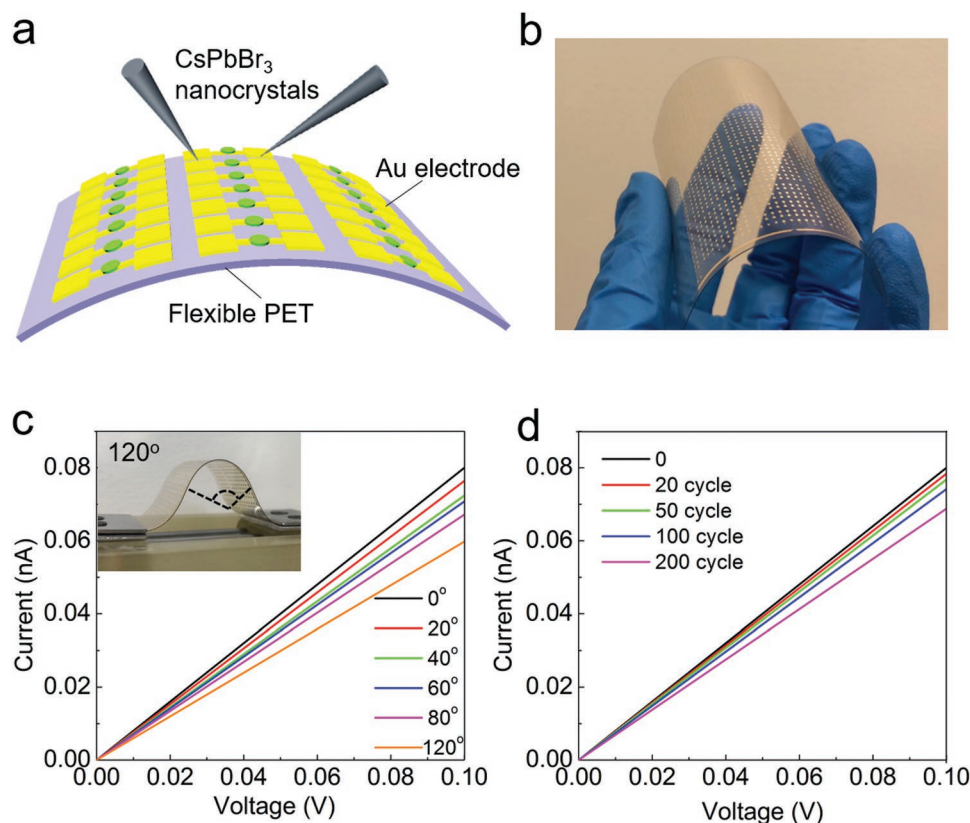


**Figure 3.** Soft-X-ray detection based on a flexible CsPbBr<sub>3</sub> QD devices. a) Schematic of the flexible perovskite based X-ray detector arrays on PET substrate. b) Photograph of flexible device under bending. c) *I*–*V* curves of the flexible device arrays at different bending angles under the X-ray illumination of 7.33 mGy<sub>air</sub> s<sup>−1</sup> and 0.1 V bias voltage. Inset: the real device showing bending in 120°. d) *I*–*V* curves of the flexible device arrays after recovering from 20, 50, 100, and 200 cycles under the X-ray illumination of 7.33 mGy<sub>air</sub> s<sup>−1</sup>.

the practical application in a reasonably long period, we tested the X-ray detector device after storing it in ambient condition for three months and found that it still worked well. Finally, it is also important to mention here that the calculated sensitivity of a flexible detector is nearly 17.7  $\mu\text{C Gy}^{-1} \text{cm}^{-2}$  which is lower than of rigid detector (i.e., 83  $\mu\text{C Gy}^{-1} \text{cm}^{-2}$ ) under same soft-X-ray dose rate of 7.33 mGy<sub>air</sub> s<sup>−1</sup> and 0.1 V bias voltage. This could be linked to a lower thickness of the film, producing less charge carriers in the flexible detector.

In conclusion, we have presented a facile approach to using solution-processed CsPbBr<sub>3</sub> QDs for the detection of the soft X-rays in which a low dose of X-ray photons was directly converted into the electrical signal. This X-ray detector can sense a very low X-ray dose rate ( $\approx 17.2 \mu\text{Gy}_{\text{air}} \text{s}^{-1}$ ) with a high sensitivity of 1450  $\mu\text{C Gy}_{\text{air}}^{-1} \text{cm}^{-2}$  at only 0.1 V bias voltage. The sensitivities achieved by this device are comparable with other perovskites X-ray detecting materials, paving the way for highly efficient products in the near future, such as medical and X-ray sensor. Moreover, a flexible X-ray detector arrays fabricated by inexpensive inkjet printing is demonstrated, which could realize the formation of a desirable pattern with a smooth surface morphology on any required substrate. The low-temperature solution processing of the CsPbBr<sub>3</sub> QDs has the unprecedented advantages of low cost and rapid synthesis, suggests a huge potential for the mass production of large-area, flexible next-generation X-ray detecting and imaging technologies.

## Experimental Section

**Synthesis of the Perovskite QDs:** The CsPbBr<sub>3</sub> QDs were synthesized by a well-developed hot injection method carrying out on a standard Schlenk line. Typically, 0.1 g Cs<sub>2</sub>CO<sub>3</sub> (307  $\mu\text{mol}$ ) was suspended in a solution of 5 mL octadecene (ODE) and 0.5 mL diisooctyl phosphonic acid (DPA) in a 50 mL three-neck flask. Meanwhile, 70 mg PbBr<sub>2</sub> (188  $\mu\text{mol}$ ) was suspended in a solution of 5 mL ODE, 0.5 mL DPA, and 0.5 mL oleylamine in a 50 mL three-neck flask. Both the two suspensions were heated to 120 °C under vacuum with stirring, with the temperature maintained for 1 h to degas. After the dissolution of the Cs<sub>2</sub>CO<sub>3</sub> and PbBr<sub>2</sub>, the temperature of the solutions was increased to 140 °C under N<sub>2</sub> and was kept for another 30 min. Then, 0.4 mL Cs precursor solution was injected into the PbBr<sub>2</sub> solution, which immediately yielded a bright green solution. After 5 s, the flask was submersed in a water bath to quench the reaction. The crude solution in ODE was then mixed with the antisolvent isopropanol in a volume ratio of ODE: IPA = 1:3, then centrifuged for 5 min at 10 000 rpm to precipitate the QDs. These QDs were free of excess ligands, avoiding the trap states that provided a pathway for the exciton recombination, which was detrimental for QD-based optoelectronic applications.<sup>[19]</sup> Afterward, the transparent supernatant was discarded and the QDs pellet was redispersed in toluene with for future usage.

**Device Fabrication:** The CsPbBr<sub>3</sub> QDs based X-ray detector devices were fabricated on SiO<sub>2</sub>/Si substrate and flexible PET substrate, respectively. First, the silica wafers with a 300 nm thick SiO<sub>2</sub> and PET substrates were rinsed in an ultrasonic bath in acetone, ethanol, and deionized water for 20 min each. Then source–drain contacts were defined on the substrate using the photolithography process with electrode array mask. After that, electrodes were deposited on the



defined region by electron-beam evaporation of Cr/Au (15/50 nm) in vacuum with a chamber pressure of  $<6 \times 10^{-6}$  Torr. The channel length between the source and drain electrodes was around 10  $\mu\text{m}$ . Finally, two copper wires were linked with two electrodes, which were used to export the photocurrent to the source meter unit (Keithley 2400 series).

**Inkjet Printing of the Perovskite Film:** The obtained QDs solution was printed onto the  $\text{SiO}_2$  substrate and flexible PET substrate by a piezoelectric inkjet printer (Fujifilm Dimatix DMP-2831) with a cartridge (10  $\mu\text{L}$  drop volume, DMC-11610). Before the printing process, the ink was ultrasonicated for 5 min to get the well-dispersed  $\text{CsPbBr}_3$  QDs solution. Then the perovskite ink was printed on the central region of each counter electrode. As the droplets evaporated, uniform and high-quality perovskite film formed on targeted regions. The size and region of each film can be controlled by the Dimatix drop manager software during the printing process. The applied jetting voltage was set between 25 and 35 V, and the frequency was set to 23 kHz. The temperature of the platen was held at 30  $^\circ\text{C}$ .

**Characterizations:** The morphologies and surface topographies were measured by the atomic force microscope (Bruker, Dimension Icon SPM). UV-vis absorbance spectra for suspensions of QDs in toluene were collected using a Perkin Elmer Lambda 950 UV-vis-NIR spectrometer. For powder XRD measurements, samples were prepared by depositing suspensions of QDs in toluene on a glass substrate and heating the substrate at 80 $^\circ$  to evaporate the toluene. XRD patterns were acquired on a Bruker D8 Advance diffractometer using a Cu source ( $K\alpha = 1.54 \text{ \AA}$ ) at 40 kV, 40 mA, and a LynxEye detector. The samples were scanned from 10 $^\circ$  to 60 $^\circ$  with a step size of 0.02 $^\circ$ . The microstructure of the sample and electron diffraction pattern were obtained by a TEM microscope (FEI, Tecnai G<sup>2</sup> T20) equipped with a LaB<sub>6</sub> electron source operated at 200 kV. Images were acquired by either a Gatan Orius SC200D CCD camera or a Gatan Orius SC600 CCD camera. The surface morphology of the sample was measured in the amplitude-modulated tapping mode. Optical images and micro-PL measurements were obtained by using a confocal microscope system (WITec, alpha 300R) with a 100 $\times$  objective lens (NA = 0.9) in ambient conditions. A 450 nm laser was used to excite samples, which was placed on a piezo-crystal-controlled scanning stage.

**X-Ray Detection:** The used X-ray source is a soft-X-ray beamline in Australia Synchrotron. The energy range is about 100–2500 eV, which is suitable for study the X-ray detecting properties of the perovskite as the X-ray radiation is effectively absorbed inside the 600 nm film. The dose rate was measured by a portable Radiation Monitor Controller (Radcal Corporation Model 9010). The effective area can refer to the focal spot size at the sample which is about 0.0006  $\text{cm}^2$ . The device with two copper wires was mounted on the sample holder with a glass slide as an insulation in between. The wires were linked with two pinholes on the sample holder, which have dedicated electrical contact to export the current to the Keithley source meter (2400 series) for the current/voltage measurement. The current vs. voltage and current vs. time were recorded by Quick IV measurement software.

For the hard-X-ray-detection measurements in the X-ray platform, the used X-ray source is the Bruker D8 discover diffractometer with Cu  $K\alpha$  Radiation (8 keV) runs at 40 kV and 40 mA. The twist tube was configured with a line beam with a spot size of 20 mm  $\times$  30 mm. Centric Eulerian cradle with rotation, tilt and X-, Y-, Z- transition for precise control of the sample position (Figure S2a, Supporting Information). In the measurement, the dose rates of the X-ray source were changed by changing the voltage (40–20 kV) and current (40–10 mA) of the Cu  $K\alpha$  Radiation source. The dose rate was measured by the Radiation Monitor Controller.

## Supporting Information

Supporting Information is available from the Wiley Online Library or from the author.

## Acknowledgements

J.L. and B.S. contributed equally to this work. The authors acknowledge the support from the National Natural Science Foundation of China (Nos. 61875139 and 51702219), the National Key Research and Development Program (No. 2016YFA0201902), Shenzhen Nanshan District Pilotage Team Program (LHTD20170006), and Australian Research Council (ARC, FT150100450, IH150100006, FT160100207, CE 170100026, and CE170100039). J.L. and Q.O. acknowledge the scholarship support from the MCATM. The authors acknowledge use of the facilities and assistance of Dr. Jisheng Ma at the Monash X-ray Platform. This research was undertaken on a soft-X-ray beamline at the Australian Synchrotron, part of ANSTO. This work was performed in part at the Melbourne Centre for Nanofabrication (MCN) in the Victorian Node of the Australian National Fabrication Facility (ANFF).

## Conflict of Interest

The authors declare no conflict of interest.

## Keywords

flexible and printable X-ray detectors, ionizing radiation, perovskites, quantum dots, soft X-rays

Received: March 15, 2019

Revised: April 22, 2019

Published online:

- [1] a) M. Spahn, *Nucl. Instrum. Methods Phys. Res., Sect. A* **2013**, 731, 57; b) M. J. Yaffe, J. A. Rowlands, *Phys. Med. Biol.* **1997**, 42, 1; c) R. Hanke, T. Fuchs, N. Uhlmann, *Nucl. Instrum. Methods Phys. Res., Sect. A* **2008**, 591, 14.
- [2] a) S. O. Kasap, J. A. Rowlands, *Proc. IEEE* **2002**, 90, 591; b) P. Büchele, M. Richter, S. F. Tedde, G. J. Matt, G. N. Ankah, R. Fischer, M. Biele, W. Metzger, S. Lilliu, O. Bikondoa, J. E. Macdonald, C. J. Brabec, T. Kraus, U. Lemmer, O. Schmidt, *Nat. Photonics* **2015**, 9, 843.
- [3] a) S. Kasap, J. B. Frey, G. Belev, O. Tousignant, H. Mani, J. Greenspan, L. Laperriere, O. Bubon, A. Reznik, G. DeCrescenzo, K. S. Karim, J. A. Rowlands, *Sensors* **2011**, 11, 5112; b) A. M. D. Ede, E. J. Morton, P. DeAntonis, *Nucl. Instrum. Methods Phys. Res., Sect. A* **2001**, 458, 7; c) C. Szeles, *Phys. Status Solidi B* **2004**, 241, 783; d) R. A. Street, S. E. Ready, F. Lemmi, K. S. Shah, P. Bennett, Y. Dmitriyev, *J. Appl. Phys.* **1999**, 86, 2660.
- [4] a) T. Takahashi, S. Watanabe, *IEEE Trans. Nucl. Sci.* **2001**, 48, 950; b) G. Zentai, L. Partain, R. Pavlyuchkova, C. Proano, M. Schieber, K. Shah, P. Bennett, L. Melekhov, H. Gilboa, *IEEE Trans. Nucl. Sci.* **2006**, 53, 2506.
- [5] H. M. Thirimanne, K. D. G. I. Jayawardena, A. J. Parnell, R. M. I. Bandara, A. Karalasingam, S. Pani, J. E. Huerdler, D. G. Lidzey, S. F. Tedde, A. Nisbet, C. A. Mills, S. R. P. Silva, *Nat. Commun.* **2018**, 9, 2926.
- [6] a) B. MacMahon, *JNCI, J. Natl. Cancer Inst.* **1962**, 28, 1173; b) K. Rothkamm, M. Löbrich, *Proc. Natl. Acad. Sci. USA* **2003**, 100, 5057; c) A. Berrington de González, S. Darby, *Lancet* **2004**, 363, 345.
- [7] a) J. Liu, Y. Xue, Z. Wang, Z.-Q. Xu, C. Zheng, B. Weber, J. Song, Y. Wang, Y. Lu, Y. Zhang, Q. Bao, *ACS Nano* **2016**, 10, 3536; b) Z. Wang, J. Liu, Z.-Q. Xu, Y. Xue, L. Jiang, J. Song, F. Huang, Y. Wang, Y. L. Zhong, Y. Zhang, Y.-B. Cheng, Q. Bao, *Nanoscale* **2016**, 8, 6258; c) J. Huang, Y. Yuan, Y. Shao, Y. Yan, *Nat. Rev.*

- Mater.* **2017**, *2*, 17042; d) Q. Ou, Y. Zhang, Z. Wang, J. A. Yuwono, R. Wang, Z. Dai, W. Li, C. Zheng, Z.-Q. Xu, X. Qi, S. Duhm, N. V. Medhekar, H. Zhang, Q. Bao, *Adv. Mater.* **2018**, *30*, 1705792; e) X. Qi, Y. Zhang, Q. Ou, S. T. Ha, C.-W. Qiu, H. Zhang, Y.-B. Cheng, Q. Xiong, Q. Bao, *Small* **2018**, *14*, 1800682.
- [8] a) Y. C. Kim, K. H. Kim, D.-Y. Son, D.-N. Jeong, J.-Y. Seo, Y. S. Choi, I. T. Han, S. Y. Lee, N.-G. Park, *Nature* **2017**, *550*, 87; b) H. Wei, Y. Fang, P. Mulligan, W. Chuirazzi, H.-H. Fang, C. Wang, B. R. Ecker, Y. Gao, M. A. Loi, L. Cao, J. Huang, *Nat. Photonics* **2016**, *10*, 333.
- [9] a) Q. Chen, J. Wu, X. Ou, B. Huang, J. Almutlaq, A. A. Zhumekenov, X. Guan, S. Han, L. Liang, Z. Yi, J. Li, X. Xie, Y. Wang, Y. Li, D. Fan, D. B. L. Teh, A. H. All, O. F. Mohammed, O. M. Bakr, T. Wu, M. Bettinelli, H. Yang, W. Huang, X. Liu, *Nature* **2018**, *561*, 88; b) J. H. Heo, D. H. Shin, J. K. Park, D. H. Kim, S. J. Lee, S. H. Im, *Adv. Mater.* **2018**, *30*, 1801743.
- [10] a) S. Yakunin, M. Sytnyk, D. Kriegner, S. Shrestha, M. Richter, G. J. Matt, H. Azimi, C. J. Brabec, J. Stangl, M. V. Kovalenko, W. Heiss, *Nat. Photonics* **2015**, *9*, 444; b) W. Pan, H. Wu, J. Luo, Z. Deng, C. Ge, C. Chen, X. Jiang, W.-J. Yin, G. Niu, L. Zhu, L. Yin, Y. Zhou, Q. Xie, X. Ke, M. Sui, J. Tang, *Nat. Photonics* **2017**, *11*, 726.
- [11] S. Shrestha, R. Fischer, G. J. Matt, P. Feldner, T. Michel, A. Osvet, I. Levchuk, B. Merle, S. Golkar, H. Chen, S. F. Tedde, O. Schmidt, R. Hock, M. Rührig, M. Göken, W. Heiss, G. Anton, C. J. Brabec, *Nat. Photonics* **2017**, *11*, 436.
- [12] a) W. Wei, Y. Zhang, Q. Xu, H. Wei, Y. Fang, Q. Wang, Y. Deng, T. Li, A. Gruverman, L. Cao, J. Huang, *Nat. Photonics* **2017**, *11*, 315; b) J. A. Steele, W. Pan, C. Martin, M. Keshavarz, E. Debroye, H. Yuan, S. Banerjee, E. Fron, D. Jonckheere, C. W. Kim, W. Baekelant, G. Niu, J. Tang, J. Vanacken, M. Van der Auweraer, J. Hofkens, M. B. J. Roeyers, *Adv. Mater.* **2018**, *30*, 1804450.
- [13] C. Zhou, Q. Ou, W. Chen, Z. Gan, J. Wang, Q. Bao, X. Wen, B. Jia, *Adv. Opt. Mater.* **2018**, *6*, 1801107.
- [14] L. Protesescu, S. Yakunin, M. I. Bodnarchuk, F. Krieg, R. Caputo, C. H. Hendon, R. X. Yang, A. Walsh, M. V. Kovalenko, *Nano Lett.* **2015**, *15*, 3692.
- [15] a) Y. Zhang, J. Liu, Z. Wang, Y. Xue, Q. Ou, L. Polavarapu, J. Zheng, X. Qi, Q. Bao, *Chem. Commun.* **2016**, *52*, 13637; b) Q.-D. Ou, C. Li, Q.-K. Wang, Y.-Q. Li, J.-X. Tang, *Adv. Mater. Interfaces* **2017**, *4*, 1600694; c) Y. Tong, E.-P. Yao, A. Manzi, E. Bladt, K. Wang, M. Döblinger, S. Bals, P. Müller-Buschbaum, A. S. Urban, L. Polavarapu, J. Feldmann, *Adv. Mater.* **2018**, *30*, 1801117.
- [16] A. W. Stevenson, C. J. Hall, S. C. Mayo, D. Hausermann, A. Maksimenko, T. E. Gureyev, Y. I. Nesterets, S. W. Wilkins, R. A. Lewis, *J. Synchrotron Radiat.* **2012**, *19*, 728.
- [17] a) B. Shabbir, M. I. Malik, N. A. Khan, *J. Supercond. Novel Magn.* **2011**, *24*, 1977; b) B. Shabbir, A. Ullah, N. Hassan, M. Irfan, N. A. Khan, *J. Supercond. Novel Magn.* **2011**, *24*, 1521.
- [18] a) B. Shabbir, H. Huang, C. Yao, Y. Ma, S. Dou, T. H. Johansen, H. Hosono, X. Wang, *Phys. Rev. Mater.* **2017**, *1*, 044805; b) B. Shabbir, M. Nadeem, Z. Dai, M. S. Fuhrer, Q.-K. Xue, X. Wang, Q. Bao, *Appl. Phys. Rev.* **2018**, *5*, 041105; c) B. Shabbir, X. Wang, Y. Ma, S. X. Dou, S. S. Yan, L. M. Mei, *Sci. Rep.* **2016**, *6*, 23044.
- [19] Y. Tong, M. Fu, E. Bladt, H. Huang, A. F. Richter, K. Wang, P. Müller-Buschbaum, S. Bals, P. Tamarat, B. Lounis, J. Feldmann, L. Polavarapu, *Angew. Chem., Int. Ed.* **2018**, *57*, 16094.